Astronomical Techniques and Instruments, Vol. 1, July 2024, 227–238

Article Open Access

# The electrical design of a membrane antenna for a lunar-based low-frequency radio telescope

**Suonanben[1,2,3,4], Fengquan Wu[3,4,5*], Kai He[3,4,5], Shijie Sun[3,4,5], Wei Zhou[6,3], Minquan Zhou[7,3], Cong Zhang[3,4,5], Jiaqin Xu[3,4,5], Qisen Yan[7,3], Shenzhe Xu[7,3], Jiacong Zhu[3,4,5], Zhao Wang[8], Ke Zhang[8], Haitao Miao[3,4,5], Jixia Li[3,4,5], Yougang Wang[3,4,5], Tianlu Chen[1,2*], Xuelei Chen[3,4,5,9,10*]**

[1]*Key Laboratory of Cosmic Rays (Tibet University)*, *Ministry of Education*, *Lhasa* 850000, *China*

[2]*Department of Physics*, *College of Science*, *Tibet University*, *Lhasa* 850000, *China*

[3]*National Astronomical Observatories*, *Chinese Academy of Sciences*, *Beijing* 100101, *China*

[4]*Key Laboratory of Radio Astronomy and Technology*, *Chinese Academy of Sciences*, *Beijing* 100101, *China*

[5]*School of Astronomy and Space Science*, *University of Chinese Academy of Sciences*, *Beijing* 100049, *China*

[6]*Shanxi University*, *Taiyuan* 030000, *China*

[7]*School of Mechanical Engineering*, *Hangzhou Dianzi University*, *Hangzhou* 310018, *China*

[8]*Center for Astronomy and Space Sciences*, *China Three Gorges University*, *Yichang* 443002, *China*

[9]*Department of Physics*, *College of Sciences*, *Northeastern University*, *Shenyang* 110819, *China*

[10]*Center of High Energy Physics*, *Peking University*, *Beijing* 100871, *China*

*Correspondences: wufq@nao.cas.cn; chentl@utibet.edu.cn; xuelei@cosmology.bao.ac.cn

Received: February 27, 2024; Accepted: April 18, 2024; Published Online: May 6, 2024; https://doi.org/10.61977/ati2024023



Citation: Suonanben, Wu, F. Q., He, K., et al. 2024. The electrical design of a membrane antenna for a lunar-based low-frequency radio telescope. *Astronomical Techniques and Instruments*, **1**(4): 227−238. https://doi.org/10.61977/ati2024023.

**Abstract:** Detecting primordial fluctuations from the cosmic dark ages requires extremely large low-frequency radio telescope arrays deployed on the far side of the Moon. The antenna of such an array must be lightweight, easily storable and transportable, deployable on a large scale, durable, and capable of good electrical performance. A membrane antenna is an excellent candidate to meet these criteria. We study the design of a low-frequency membrane antenna for a lunar-based low-frequency (<30 MHz) radio telescope constructed from polyimide film widely used in aerospace applications, owing to its excellent dielectric properties and high stability as a substrate material. We first design and optimize an antenna in free space through dipole deformation and coupling principles, then simulate an antenna on the lunar surface with a simple lunar soil model, yielding an efficiency greater than 90% in the range of 12–19 MHz and greater than 10% in the range of 5–35 MHz. The antenna inherits the omni-directional radiation pattern of a simple dipole antenna in the 5–30 MHz frequency band, giving a large field of view and allowing detection of the 21 cm global signal when used alone. A demonstration prototype is constructed, and its measured electrical property is found to be consistent with simulated results using $|S_{11}|$ measurements. This membrane antenna can potentially fulfill the requirements of a lunar low-frequency array, establishing a solid technical foundation for future large-scale arrays for exploring the cosmic dark ages.

**Keywords:** Membrane antenna; Lunar-based radio array; Cosmic dark ages

## 1. INTRODUCTION

The concept of building a radio astronomical observatory on the far side of the moon has been considered since as early as 1965[1]. This is especially vital for the frequency band below 30 MHz, which remains largely unexplored because ground-based observations are severely affected by the strong reflection and absorption of Earth's ionosphere, together with ubiquitous radio frequency interference (RFI). Conducting low-frequency radio observations on the lunar far side or in lunar orbit not only avoids the influence of Earth's ionosphere but also leverages the moon's shielding to block the otherwise substantial terrestrial electromagnetic interference[2]. The opening up of this new window of astronomical observation holds vast potential for new discoveries and promises great scientific value. One of the most fascinating poten-

tial uses of such a telescope is the observation of the cosmic dark ages. This is the era after recombination of the hot plasma following the Big Bang, and before the formation of first generation stars and galaxies[3]. The exploration and study of the cosmic dark ages may give insights into the early evolution of the universe and the nature of dark matter and offer the opportunity to observe primordial fluctuations generated during the inflationary era before their non-linear evolution, elucidating the origin of the universe[4-6]. Additionally, the ultra-long wave band can also be used for researching solar radio emissions, exoplanet radio emissions, the solar system's local environment in the galaxy, galaxy medium distribution, and the origins of cosmic rays, among other subjects[7].

In 1972, the US RAE-2 satellite, equipped with a low-frequency inverted-V antenna, carried out observations of ultra-long wave signals in lunar orbit, confirming extreme electromagnetic quietness on the lunar far side[8]. Subsequently, a number of spacecraft have carried low-frequency payloads to make space-based observations, primarily aimed at solar or planetary sources (e.g., [2,6,7] for further discussions). During the Chinese Chang'e 4 mission, low-frequency radio experiments have also been carried out by the lander[9], the relay satellite[10], and the Longjiang 2 lunar micro-satellite[11].

Currently, a number of lunar radio astronomy mission concepts are under development, including lunar orbit single satellites such as The Dark Ages Polarimeter Pathfinder (DAPPER)[12], or satellite arrays like Discovering Sky at the Longest Wavelength (DSL)[13-16]. It is also a consideration in lunar surface project concepts, such as the Lunar Surface Electromagnetics Experiment (LuSEE)[17], the Lunar Crater Radio Telescope (LCRT)[18], and the Farside Array for Radio Science Investigations of the Dark ages and Exoplanets (FARSIDE)[12] proposed by the USA, the Astronomical Lunar Observatory (ALO) project[6], and the Large Array for Radio Astronomy on the Farside (LARAF) proposed by China[19]. Projects based in lunar orbit are typically simpler in terms of space engineering, but the lunar surface provides certain advantages; telescopes can be deployed on solid ground, making control, communication, and data analysis simpler, especially if they include a large number of array elements.

Constructing a radio telescope with a large receiving area and a large number of elements on the lunar far side surface is a great engineering challenge due to the prohibitive expense of shipping the material to the Moon and the severely restricted amount of labor and tools available for deployment and construction. A logical way to alleviate these problems is to construct the antenna using thin films, which are lightweight and easy to fold and store for shipping[20]. Unlike on Earth, where a film needs to be fastened against the wind, lunar deployment is simplified by the lack of a significant lunar atmosphere. This is therefore considered as a major design option for most current lunar surface low-frequency radio astronomy projects[21-23]. Membrane antennas have previously also been used on Earth for other applications (e.g., cellphone antennas or biomedical antennas), though typically on a much smaller scale[24].

In this paper, we conduct a preliminary study on the electrical design and performance of a membrane antenna in the context of constructing a lunar surface low-frequency array. The paper is organized as follows: in Section 2, we present the design of the membrane antenna; in Section 3, we describe our electromagnetic simulation and experiment test. We summarize and conclude in Section 4.

## 2. ELECTRICAL DESIGN OF A MEMBRANE ANTENNA

A lunar surface radio telescope can either be a reflector, such as the LCRT[18], an array of dipoles, or any variation or combination of these. A membrane can be applied in the construction of any type. Here we primarily consider the dipole array type, which is simpler to deploy and construct and is more flexible for large-scale applications. The membrane itself can be made with printed conducting layers, which can function as the antenna or connection wire. Being lightweight, a relatively large geometric size can be achieved, at least along one dimension. Before deployment, the membrane can be rolled to reduce its size for storage. It can then be carried by a lunar rover to the desired site, before being unrolled onto the lunar surface. A number of materials can be used for making such a membrane. Polyimide film, for example, exhibits excellent electrical properties ($\varepsilon$ from 3.1 to 3.5, tan$\delta$ from 0.001 to 0.01) and has good stability in the ambient temperature extremes of the lunar surface[25]. Consequently, we selected it as the antenna substrate considered in this study.

In the design of membrane antennas, apart from seeking a larger impedance-matched bandwidth, some engineering and technical specifications must also be satisfied. Here, we assume that for the convenience of rapid deployment on the far side of the moon, using a reel on the lunar rover, the width of the antenna is limited, i.e., we assume the film is a long strip. Wider films will require special design to fold and deploy, which we do not consider here.

### 2.1. Simple Dipole Antennas

We start with a simple dipole antenna made with the membrane, as shown in Fig. 1A, with a length of 20 m, and a thickness of less than 1 mm, and a feed port impedance of 50 Ω. We consider a number of different widths, including 0.01 m, 0.25 m, 0.5 m, 0.75 m, and 1 m. On each, we perform an electromagnetic simulation of its electric performance, first in free space, then with a lunar surface model (described in Section 3.2) to investigate its impact on the dipole antenna.

The simulation results of the $|S_{11}|$ parameter, shown in Fig. 2, demonstrate that simple dipoles exhibit narrow resonances in free space. Fig. 2A compares dipoles with di-

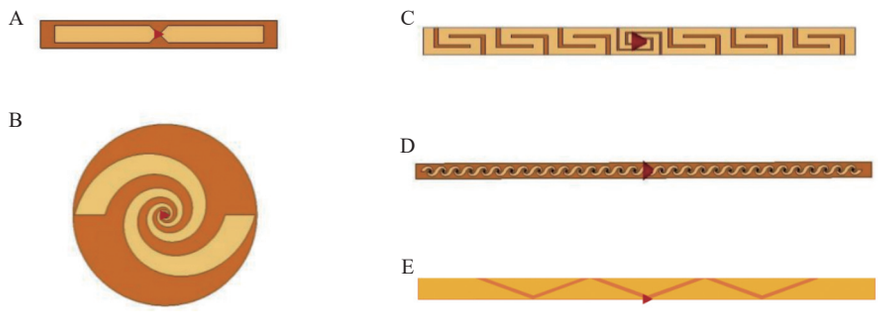


**Fig. 1. Several designs of membrane antennas.** (A) Dipole. (B) Logarithmic spiral. (C) Square spiral dipole. (D) Helical dipole. (E) Planar-coupled dipole. The red arrows show the feed port of each antenna.

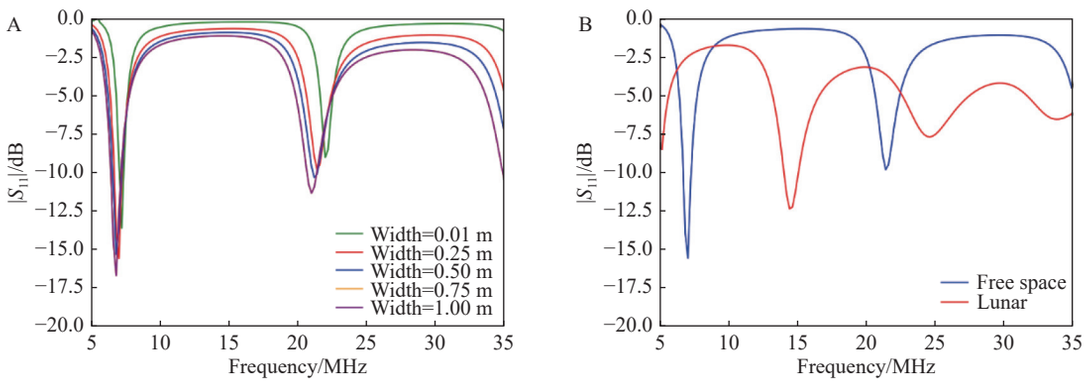


**Fig. 2. $|S_{11}|$ of the dipole membrane antenna.** (A) Different width in free space. (B) Comparison of the 0.25 m width dipole in free space and with lunar ground.

fferent widths in free space. The thinnest has the narrowest resonances, with the fundamental frequency occurring where the total length is equal to $\lambda/2$ (for $\lambda/2$ = 20 m, the corresponding frequency is 7.5 MHz). Higher resonances are observed at odd multiples of the fundamental frequency, with the next falling at 3 × 7.5 MHz = 22.5 MHz. For dipoles with larger widths, resonance frequencies are lower, with broader widths. We select the 0.25 m width model as our reference model, with its resonance occurring at approximately 7 MHz.

We observe that under the influence of the lunar surface (Fig. 2B), the resonance points of the dipole antenna shift to lower frequencies than those in free space. This is because the lunar surface environment increases the effective permittivity of the environment in which the dipole is located, compared with free space.

Simulated antenna beam patterns are shown in Fig. 3 for free space, and Fig. 4 for the lunar surface. In free space, the antenna maintains a broad dipole pattern. As the frequency increases, the two-lobed beam pattern splits into four lobes, due to the reverse currents on the antenna at shorter wavelengths. The presence of the lunar surface causes the antenna pattern under the lunar surface almost disappear. Owing to the effect of surface loss, the peak gain of the dipole antenna on the lunar surface is usually below 0 dBi. At higher frequencies, the antenna pattern will split further, giving more lobes.

## 2.2. Design Schemes of Membrane Antennas

A simple dipole has a narrow working band which requires a small $|S_{11}|$, making it not very suitable for the purpose of observing low frequencies in a range of astronomical applications. This is a general problem in the design of low-frequency receivers. These have a large relative variation of frequencies, making it difficult to maintain well-matched impedance of the antenna and receiver over a wide frequency range. Here, we try to design a system to achieve good impedance matching over a relatively wide bandwidth.

In the design process, we first improve and optimize the antenna structure with various design patterns. We initially considered adopting the logarithmic spiral structure (Fig. 1B), with a feed port impedance of 200 Ω, capable of achieving ultra-wide band matching. However, for storage and deployment on the Moon by a single rover, a long strip of film wrapped around a spool is the most convenient form to use. With this in mind, we devote most of this study to designs in this form, such as the dipole square spiral and helical dipole, as shown in Fig. 1C, D. However, these still require a large width to work effectively.

We find that the planar-coupled design can effectively expand the bandwidth of the antenna. Planar coupling refers to certain conductive layer portions of the antenna that are not directly connected, but are designed around the antenna to change its impedance through interaction of the electromagnetic field. The additional radiation paths and effective electromagnetic modes are significantly increased by the planar-coupled structure, thereby expanding the bandwidth of the antenna[26]. By using a

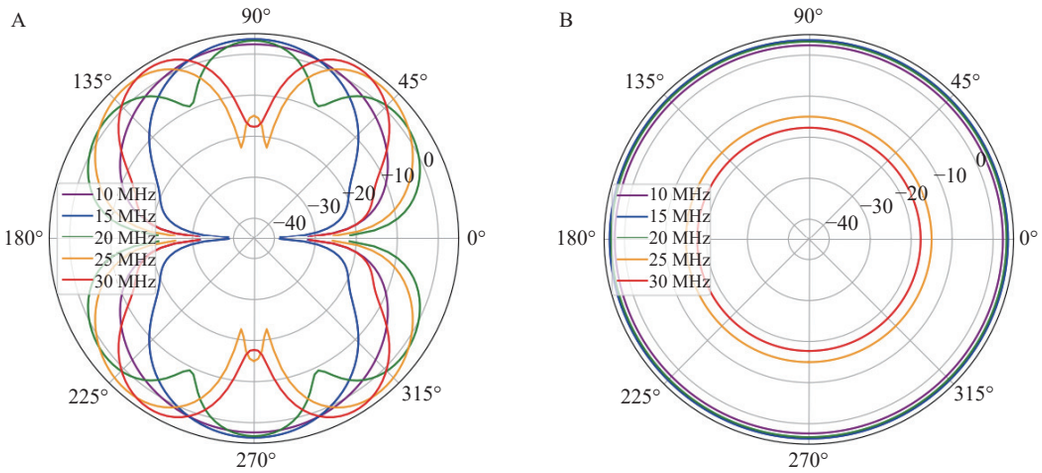


**Fig. 3. The beam patterns of the dipole model on the E-plane (A) and H-plane (B), simulated in free space.**

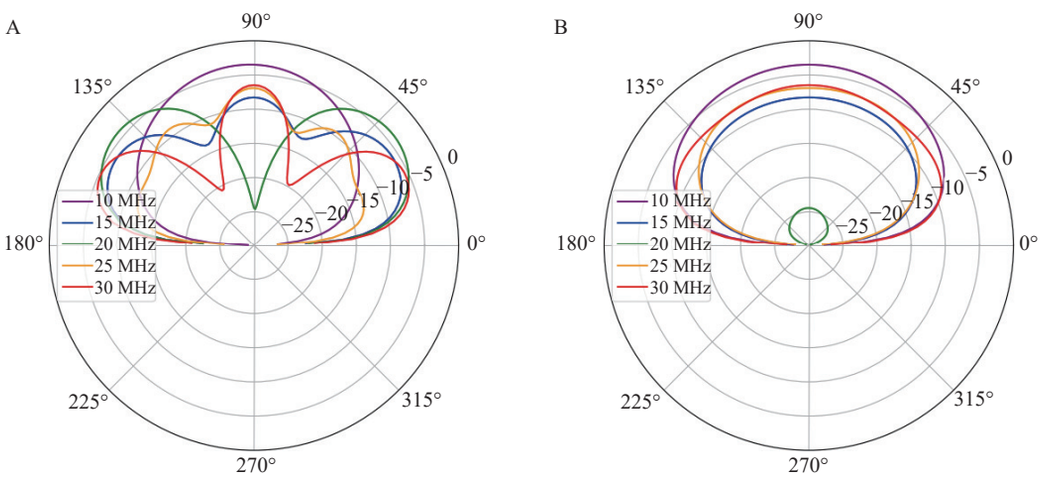


**Fig. 4. The beam patterns of the dipole model on the E-plane (A) and H-plane (B), simulated on a modeled lunar surface.**

balun for impedance transformation, a planar-coupled wide-band dipole membrane antenna can be a good candidate. A possible design is shown in Fig. 1E. Two triangular regions at the bottom of the center are radiation blades, and other areas are planar-coupled structure which are not connected with each other. The feed port impedance is 300 Ω.

To simplify the simulation process and reduce simulation time, we first consider the free space background for the membrane antenna design and parameter optimization. Performance and optimization of the membrane antenna are then discussed and optimized with a simple lunar soil model, based on current lunar measurement data.

## 2.3. Parameter Optimization

After extensive simulations using the Computer Simulation Technology (CST) and FEKO (FEldberechnung bei Körpern mit beliebiger Oberfläche) software suites, on a number of different designs, we propose a lightweight, foldable, planar-coupled design. The main body of the membrane antenna is made up of isosceles triangular-shaped structures of conducting area, with a connection balun placed directly beneath the center. The remaining triangular structures are not connected but they alter the antenna impedance through planar coupling, thereby extending the antenna's impedance bandwidth. This allows the membrane antenna, though a geometrically narrow structure, to have a large impedance bandwidth.

The sizes of various structures and thickness of the membrane antenna are marked in Fig. 5 and given in Table 1. The base material use for the bottom layer of the membrane is polyimide. The middle layer is metallic copper acting as the radiating layer, and the top layer is a coating layer used for preventing copper oxidation. Because this top layer is very thin, it is difficult for the software to simulate it accurately. Because the top layer of paint has minimal impact on the thin-film antenna, it is omitted from the simulation. An aerial photograph of the actual prototype, placed on the ground, is shown in the Fig. 6.

The size of the membrane antenna is determined by several parameters. We focus on scanning and optimizing a few primary parameters, with the impedance bandwidth serving as the principal criterion, to achieve a larger impedance bandwidth below 30 MHz, and employ the CST simulation software for parameter scanning. Fig. 7 dis-

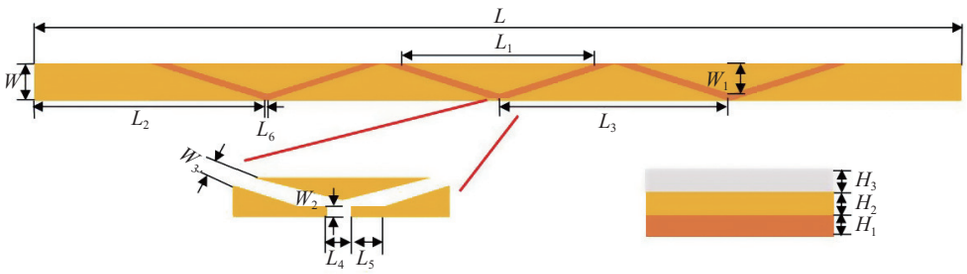


**Fig. 5. Geometric structure of the membrane antenna.**

**Table 1. Dimensions of the membrane antenna**

| Parameters | Size/cm | Parameters | Size/cm |
|---|---|---|---|
| $L$ | 20000 | $W$ | 25 |
| $L_1$ | 400 | $W_1$ | 20 |
| $L_2$ | 499.5 | $W_2$ | 1 |
| $L_3$ | 499 | $W_3$ | 4.6 |
| $L_4$ | 1 | $H_1$ | $1.2\times10^{-3}$ |
| $L_5$ | 1 | $H_2$ | $1.2\times10^{-3}$ |
| $L_6$ | 1 | $H_3$ | <0.1 |

plays the $|S_{11}|$ result of the different $L_1$, $W$, $W_1$, $L_2$, and $L_3$ parameters. We find that for the optimal parameter set, $L_1$ = 400 cm, $W_1$ = 20 cm, $L_2$ = 499.5 cm, and $L_3$ = 499 cm. For this parameter set, the bandwidth for which $|S_{11}| < -10$ dB is the widest ranging from 15 MHz to 27 MHz. In addition, the simulation results show that increasing the width of the membrane antenna, $W$, improves $|S_{11}|$, further broadening the bandwidth. However, the width is necessarily constrained by practical engineering specifications, and the antenna therefore cannot be overly wide.

### 2.4. Balun

The membrane antenna requires a balun structure for balanced-to-unbalanced conversion, as well as impedance transformation. With many types of balun structures available, choosing a suitable design is crucial to the performance of the antenna. A transformer balun exhibits superior performance in this band and can achieve an ultra-large bandwidth, so choose this variety of balun for the membrane antenna and use impedance transformation to widen the impedance bandwidth.

The test model of transformer used here is a MABA-011040, manufactured by MACOM, with an impedance transformation ratio of 1:6. Fig. 8 shows a photograph of the transformer balun, with dimensions $L_7$ = 2.4 cm and $W_4$ = 3.1 cm. The size of the balun was minimized to reduce insertion loss and lessen the impact on the mechanical structure of the membrane antenna. Measurement of the balun's S-parameters was performed using a back-to-back cascade approach with a Copper Mountain TR1300/1 vector network analyzer (VNA). Fig. 9 shows that $|S_{11}| < -18$ dB, and $|S_{21}| > -0.55$ dB across the entire frequency band. The 1:6 transformer balun exhibits excellent impedance matching and low transmission loss, meeting the requirements of the membrane antenna for an ultra-wide band.

## 3. SIMULATION

Here, we consider simulations of our antenna models. We first make a validation test by simulating a membrane antenna model on the terrestrial ground, which can be compared with the measurement data. We then describe the model for the lunar soil and use it to simulate the performance of the antenna on the lunar surface.

### 3.1. Terrestrial Validation Test

We first validate our simulation by using terrestrial measurements of the membrane antenna. A membrane antenna with a feed port impedance of 300 Ω is connected via a 1:6 impedance-transforming balun transformer and tested in an open field near the Hongliuxia Observatory in Balikun County, Xinjiang, where the Tianlai experiment is located[27]. The $|S_{11}|$ parameter is measured with a portable VNA. The relative permittivity and conductivity of the ground at the site are also measured. The measurement of the relative dielectric constant is conducted using the Time Domain Reflectometry method[28], and the conductivity measurement is performed using the Four-point probe method originally developed for semi-conductor material [29]. We model the testing site ground as

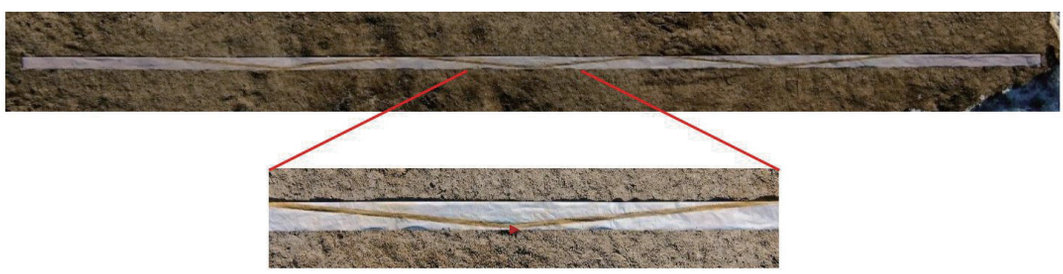

**Fig. 6. Aerial photograph of a membrane prototype antenna, taken by a drone.**

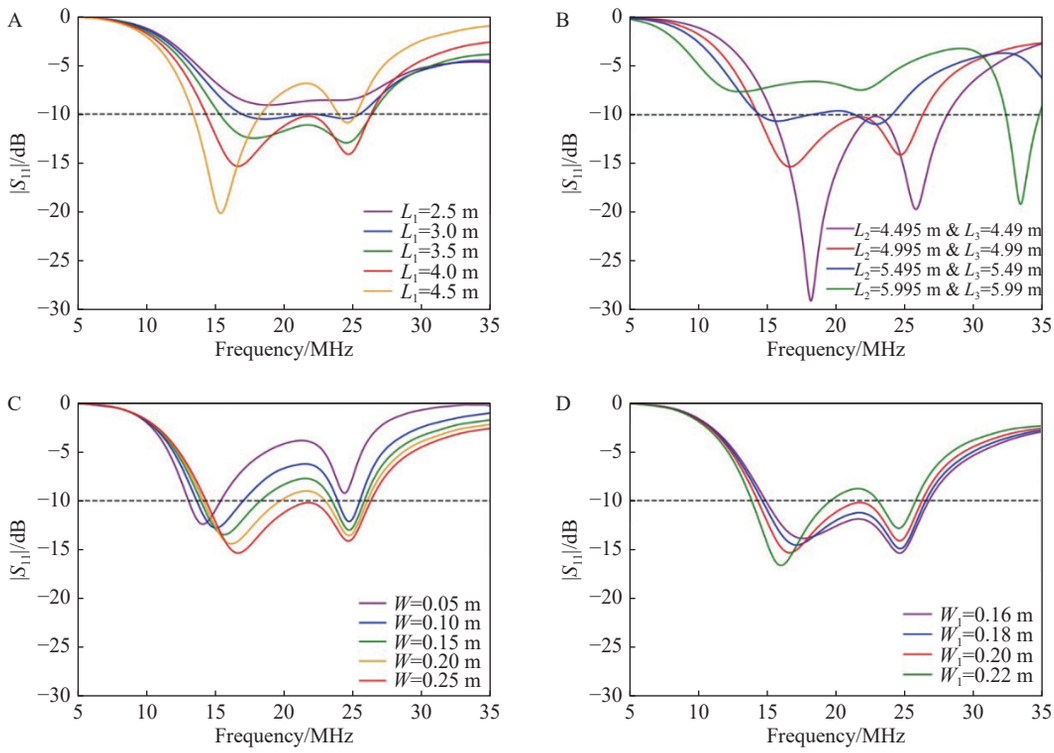


**Fig. 7. Optimization of membrane antenna parameters.** (A) The parameter scan of $L_1$. (B) The parameter scans of $L_2$ and $L_3$. (C) The parameter scan of $W$. (D)The parameter scan of $W_1$. The red curve represents the optimal parameter set.

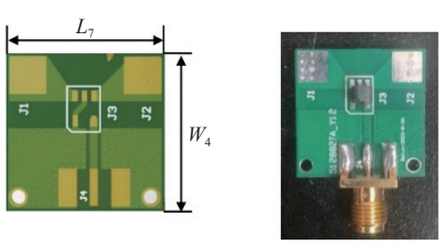


**Fig. 8. Illustration of the impedance-transforming balun, showing physical dimensions, and a photograph of the balun used.**

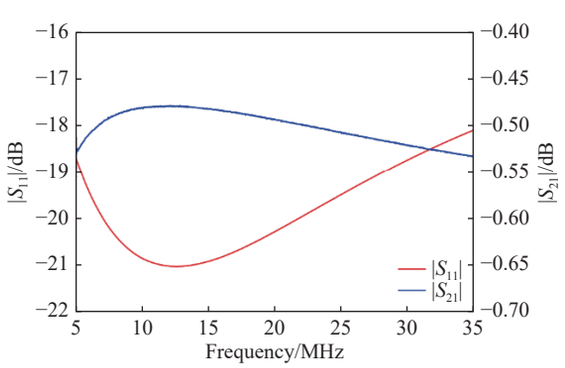


**Fig. 9. S-parameter measurement of the balun. The red and blue lines represent $|S_{11}|$ and $|S_{21}|$, respectively.**

an infinitely large ground plane, with the underground filled by a media with a relative permittivity of 3.60 and a conductivity of 0.064 S/m, per our measurements.

Fig. 10 shows terrestrial measurement and simulation results, showing that the measured $|S_{11}|$ is below −5 dB in the 10–35 MHz frequency band, with a resonance point at around 13 MHz. This is generally consistent with the simulation, though there is still some difference in the magnitude of $|S_{11}|$, probably due to the simplification of the ground model. Real soil may have different conductivity and permittivity at different depths, leading to some discrepancy between the simulation and real measurements. This general agreement between the ground measurement and simulation gives us confidence that we can use the simulation for our design, provided we use a reasonably good lunar surface model.

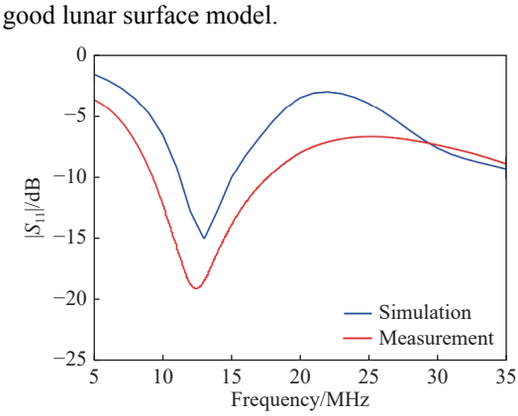


**Fig. 10. The measured $|S_{11}|$ on the ground.**

### 3.2. The Lunar Surface Model

To use the membrane antennas on the surface of the moon, it is necessary to understand the impact of the dielectric properties of lunar soil on its performance.

The dielectric constant is a complex number

$$\varepsilon = \varepsilon' - \mathrm{i}\varepsilon'' = \varepsilon_0\left(\varepsilon_\mathrm{r} - \mathrm{i}\frac{\sigma}{\omega\varepsilon_0}\right), \tag{1}$$

where $\varepsilon'$ is the real part of the complex dielectric constant, $\varepsilon''$ is the imaginary part, $\varepsilon_0$ is the vacuum permittivity, $\varepsilon_\mathrm{r}$ is the relative permittivity, $\sigma$ is the electrical conductivity, and $\omega$ is the angular frequency.

The imaginary part of the permittivity is generally characterized using the loss tangent, defined as

$$\tan\delta = \frac{\varepsilon''}{\varepsilon'}. \tag{2}$$

The dielectric properties of lunar surface materials vary with different locations and depths. From existing research on the dielectric properties of lunar samples obtained from the Apollo and Luna missions[30], the real part of the permittivity of lunar soil is primarily related to density, showing little correlation with chemical composition and mineral constituents, while the loss tangent is associated with density and the proportion of FeO and $TiO_2$[30], as

$$\begin{aligned} &\varepsilon_\mathrm{r} = 1.919^{\rho} \\ &\tan\delta = 10^{0.440\rho - 2.943} \\ &\tan\delta = 10^{0.038(\mathrm{FeO}+\mathrm{TiO_2})\%+0.312\rho-3.26} \end{aligned}. \tag{3}$$

Recent Chinese lunar missions, namely Chang'e 3, 4, and 5, use ground-penetrating radar to infer the complex permittivity of the lunar surface, yielding similar results[31-33]. Chang'e 4, in particular, was the first to land on the far side of the moon, offering valuable reference data for future low-frequency exploration. Chang'e 4 measured the complex dielectric constants of the lunar surface down to a depth of 10 m, showing the relative permittivity to be between 2.64 and 3.85, with a loss tangent between 0.0032 and 0.0044[31]. Chang'e 6 is intended to return the first soil samples from the lunar far side, potentially allowing the lunar surface model to be further improved as new data becomes available.

The permittivities of lunar samples have been measured at frequencies of 0.1 MHz, 1 MHz, and 450 MHz[30]. As shown in Fig. 11, the measured permittivities of lunar samples at 0.1 MHz and 1 MHz are generally in line with the above formula derived from the bulk samples, with the relative permittivity showing a strong correlation with density.

The loss tangent also increases with density, although the correlation is not as strong. It is also related to the material content, particularly the ilmenite concentration [9]. The loss tangent also changes with frequency, with the lowest resonant point occurring around 10 MHz, which is also temperature-dependent [30]. On the whole, the loss tangent on the lunar surface is extremely small, indicating excellent insulation and suggesting that the radiation efficiency of membrane antennas would not be much affected.

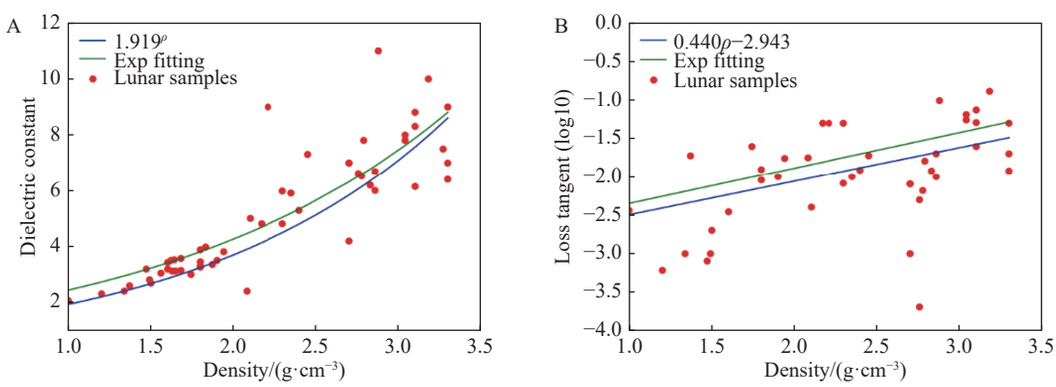


**Fig. 11. The relative permittivity (A) and loss tangent (B) of lunar soil as a function of density.**

The lunar surface material consists of both regolith and rocks. Here, we model it as two plane layers, using the FEKO infinite multilayered medium simulation. The first layer consists of weathered regolith, which typically has an average thickness of 4–5 m in lunar maria and 10–15 m in highland regions[34]. Here we consider the average thickness of 8.5 m, with density increasing gradually from 1.49 at the surface to 2.07 g·cm$^{-3}$ at a depth of 8.5 m. With depth, the corresponding relative permittivity increases from 2.64 to 3.85[31], with an average value of 3.25. This aligns with the sample's average loss tangent of 0.009 1. The second layer, the rock layer, is modeled with an effectively infinite thickness. Its complex permittivity is primarily derived from Chang'e 4's ground-penetrating radar measurements, with a density in the range of 2–2.6 g·cm$^{-3}$ at depths of 10–45 m. The average relative permittivity is taken to be 5.61, based on the data presented in Fig. 11, with a loss tangent of 0.0246 and thickness taken as infinite. This structure is illustrated in Fig. 12.

### 3.3. Simulation with the Modeled Lunar Surface

For a simulation in free space, the $|S_{11}|$ parameter and power beam pattern are shown in Fig. 13, yielding $|S_{11}|$ below −10 dB in the 15–27 MHz frequency band with a relative bandwidth of 57%. As the membrane antenna designed in this work is a type of dipole antenna, the directional pattern is essentially consistent with that of a dipole, maintaining a characteristic wide beam throughout the entire frequency band with a peak gain of about

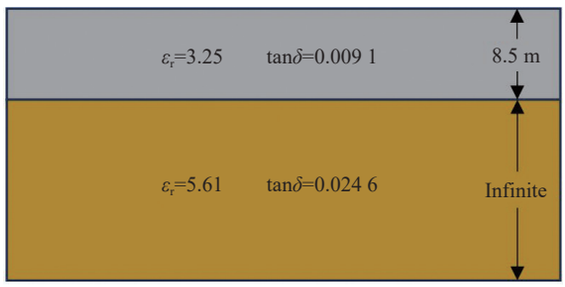


**Fig. 12. Schematic diagram showing a simplified lunar surface structure model, with relative permittivities and loss tangents.**

2.5 dBi. The E-plane directional pattern splits slightly at the maximum frequency of 30 MHz. This occurs because the antenna size exceeds the half wavelength, resulting in the splitting of the main lobe due to the presence of reverse currents, though the direction of the lobes does not change significantly. The H-plane directional pattern is essentially omni-directional in the entire frequency band.

Our simulation uses the simplified lunar surface model described above, in Section 3.2. Fig. 14A shows the simulated antenna impedance, including both real and imaginary parts. For most of the frequency range, the imaginary part is negative, giving a mostly capacitive impedance. Fig. 14B shows $|S_{11}|$ under different reference impedances. The widest impedance-matching bandwidth with $|S_{11}| < -10$ dB is achieved when the impedance transformation ratio is 1:4 on the lunar surface. $|S_{11}|$ is below −10 dB within the frequency range of 11–18 MHz, yielding a relative bandwidth of 48.2%. However, as mentioned before, the maximum impedance bandwidth occurs under a 1:6 impedance transformation in free space, indicating that the optimal balun impedance transformation ratio varies between free space and the lunar surface.

In the simplified lunar surface model, shown in Fig. 12, the dielectric properties of the first layer of lunar soil (or regolith) predominantly affect the performance of the membrane antenna. However, because the dielectric properties of the lunar surface vary with location and depth, we examine a range of relative permittivities and loss tangents. Fig. 15 shows the influence of complex dielectric properties on the performance of the membrane antenna on the lunar surface. The relative permittivity affects the $|S_{11}|$ parameter of the antenna significantly. As it increases, the resonance points shift toward lower frequencies, as expected. The influence of the loss tangent on $|S_{11}|$ is less noticeable, mainly due to the very low loss tangent value of the regolith. Observable changes only occur when they reach to a threshold level.

Simulated beam patterns are shown in Fig. 16, peaking in the zenith direction with a peak gain less than 1 dBi, somewhat smaller than the free space case due to

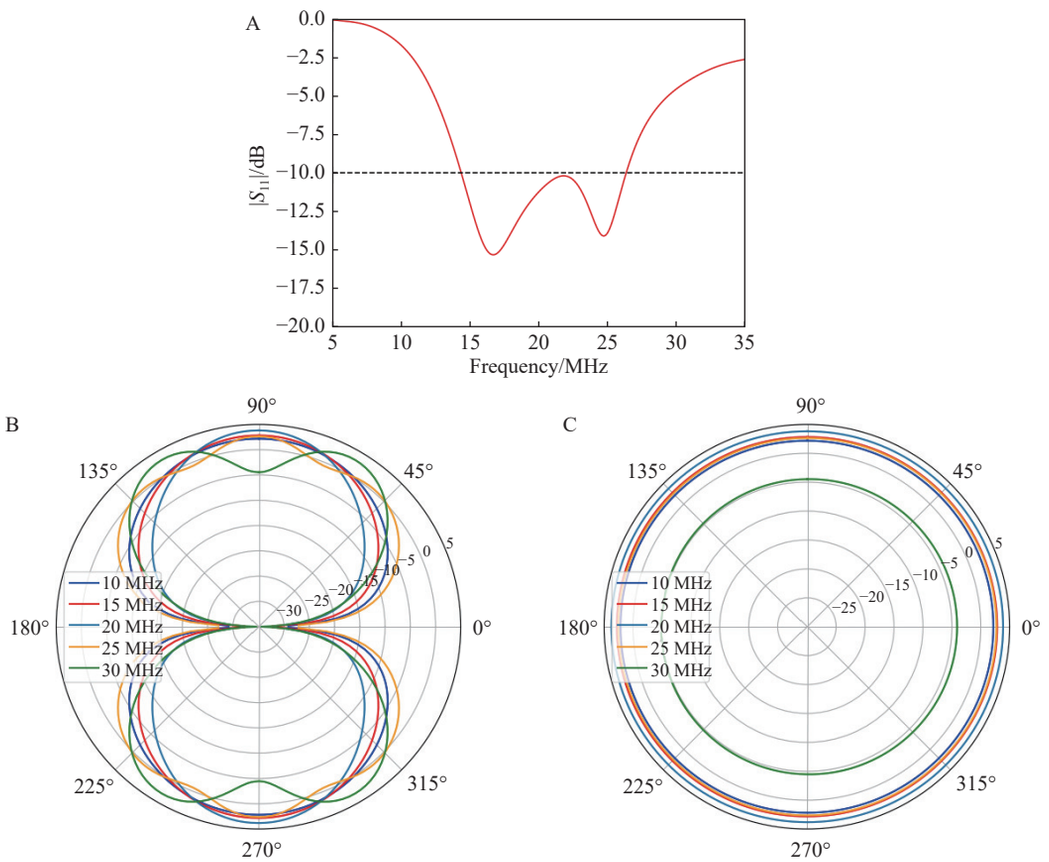


**Fig. 13. Simulation results for a membrane antenna in free space.** (A) The $|S_{11}|$ parameter. (B) The power beam pattern in the E-plane. (C) The power beam pattern in the H-plane.

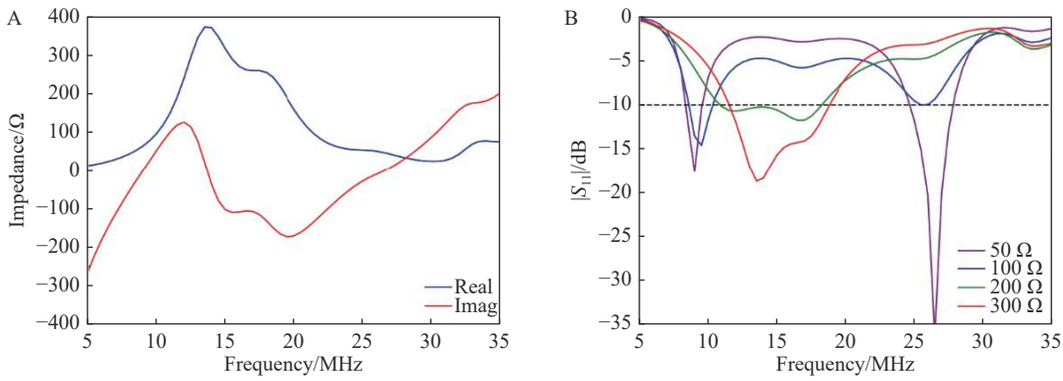


**Fig. 14. (A) Antenna impedance on the lunar surface. (B) $|S_{11}|$ for various reference impedance values.**

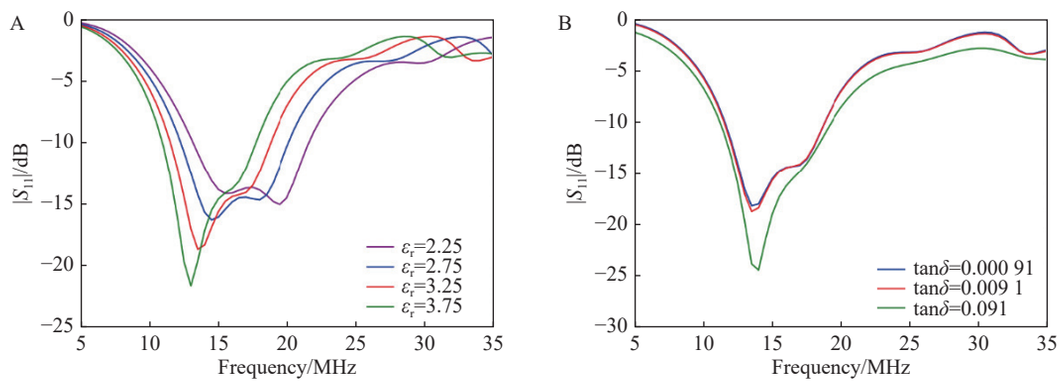


**Fig. 15. Comparison of $|S_{11}|$ for different relative permittivity (A) and loss tangent (B).**

Ohmic loss on the lunar surface. There are some ripples modulating on top of the dipole pattern due to apparent chromaticity, i.e., the beam pattern changes with frequency. These effects are relatively minor and can be easily accommodated in conventional astronomical observations. However, observation of 21 cm fluctuations in the cosmic dark ages requires extremely high precision, and such variations and ripples may introduce complications. Further efforts will be required to compensate for these effects.

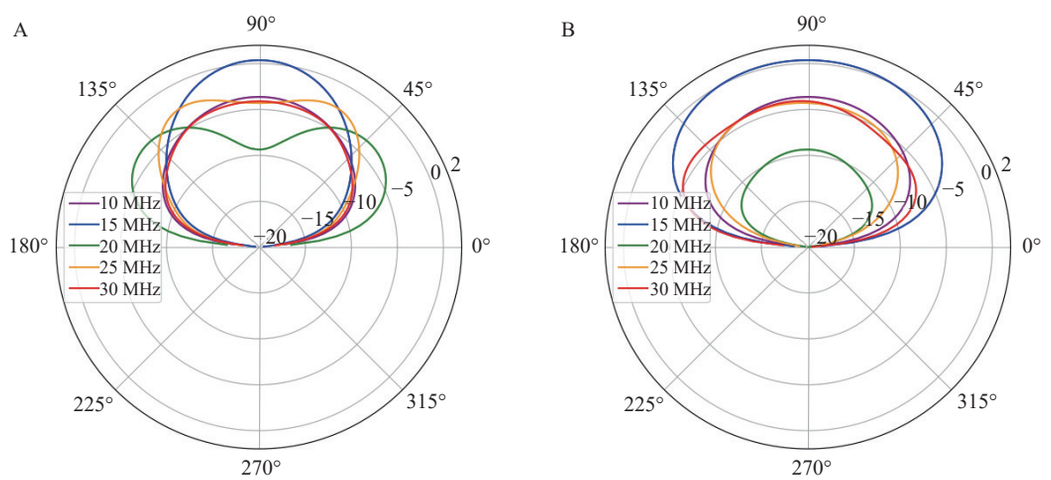


**Fig. 16. The beam pattern of the membrane antenna model.** (A) The E-plane. (B) H-plane.

Fig. 17 shows the impact of different permittivity values on the beam pattern at 15 MHz. An increase in relative permittivity results in increased ground loss and decreased gain for the membrane antenna in both the E-plane and the H-plane.

The pattern also changes with variation of the loss tangent, as shown in Fig. 18, with an increase in loss tangent leading to a weak decrease in antenna gain. This influence is negligible while the loss tangent is below a threshold level, becoming very obvious at higher values.

### 3.4. Antenna Efficiency

Antenna efficiency here is determined primarily by antenna Ohmic loss, ground loss, and impedance mismatch-

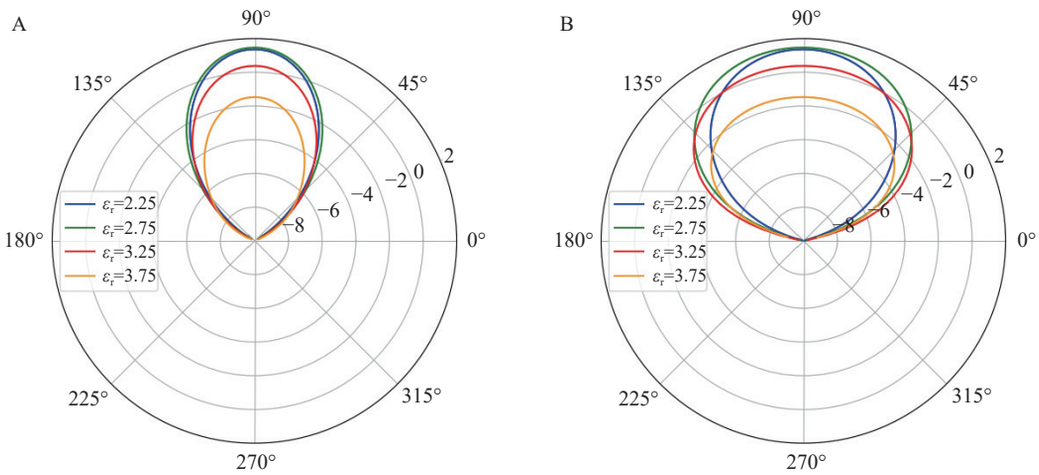


**Fig. 17. Effects of relative permittivity on beam pattern .** (A) The E-plane. (B) H-plane.

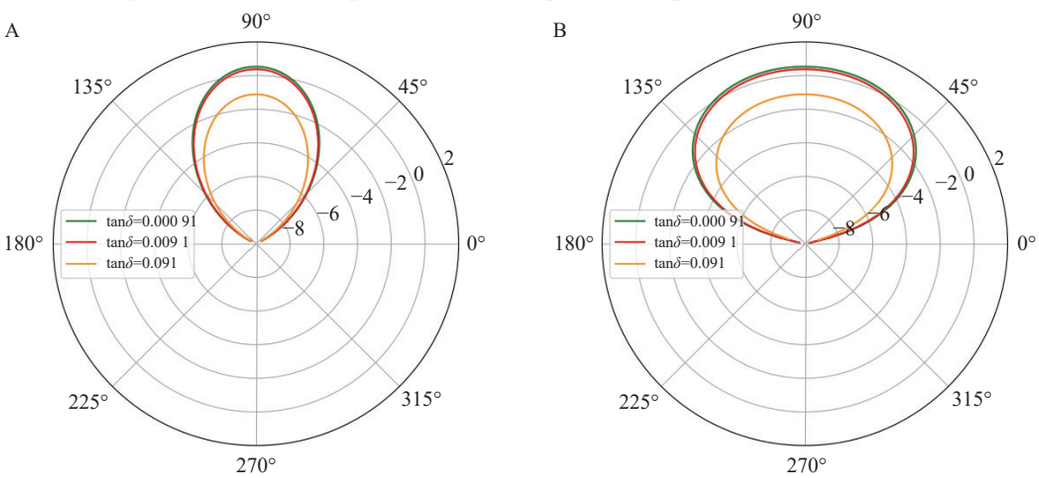


**Fig. 18. Effects of the loss tangent on beam pattern.** (A) The E-plane. (B) H-plane.

ing. For a membrane antenna on the lunar surface, Ohmic loss and ground loss are both small, making impedance mismatching the dominant consideration for antenna efficiency. Efficiency from impedance mismatching is calculated using the relationship

$$\eta = 1 - \left|\Gamma^2\right|, \tag{4}$$

where $\eta$ is the antenna efficiency and $\Gamma$ is the reflection coefficient.

For frequency bands below 35 MHz, the sky signal mostly comes from the synchrotron radiation of the Milky Way. The brightness temperature of this synchrotron radiation exceeds ~$10^4$ K at 30 MHz and can be in excess of ~$10^7$ K at a few MHz, so it is the dominant component of system temperature. For an antenna efficiency of 10%, the signal-induced antenna temperature still far exceeds the environment temperature of the system, so a good signal-to-noise ratio can still be obtained. We take the bandwidth at 10% antenna efficiency as a workable bandwidth for the lunar antenna.

Fig. 19 shows a comparison between the efficiency in free space and on the lunar surface, indicating that this membrane antenna can achieve an efficiency greater than

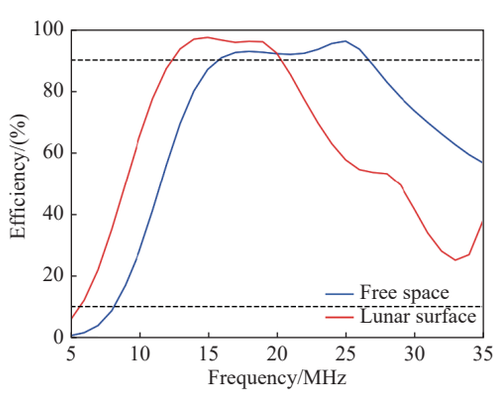


**Fig. 19. Comparison of antenna efficiency of membrane antennas in free space and on the lunar surface.**

10% in free space at 7.4–35 MHz and an efficiency greater than 90% at 15–27 MHz. The lunar surface simulation results show that the membrane antenna's efficiency exceeds 10% at 5–35 MHz and 90% at 12–19 MHz.

## 4. SUMMARY

Lunar-based radio astronomy, as an important astronom-

ical goal, is crucial for studying the epochs of the Cosmic Dark Ages and Cosmic Dawn. In such projects, the membrane antenna could play an important role. It has a number of favorable properties, such as light weight, compact collection volume, easy deployment, and no need to be fastened against wind in the lunar environment, making it well suited for use on a lunar mission. The receiving circuit can be directly mounted on the membrane antenna, forming an integrated receiver.

In this study, we investigate the electrical design of membrane antennas, noting that polyimide films have been used for previous space-based applications. However, in using this material for an antenna on the lunar surface, performance and durability still need to be investigated under the extreme variations in temperature and radiation exposure present on the surface of the moon. The goal is to construct a large radio interferometer array for ultra-long-wavelength astronomy, i.e., at frequencies below 30 MHz. The antenna unit must have a wide beam and a broad working bandwidth, in order for the array to achieve a large field of view with the potential to be used in a wide variety of astronomical research, including observing the early universe. Here, we primarily consider designs in the form of a long, narrow strip, as the most practical form to store, transport, and deploy.

Our antenna adopts a planar-coupling broadband dipole design, capable of achieving an antenna efficiency greater than 10% in free space from 7.4–35 MHz and greater than 90% antenna efficiency from 15–27 MHz while maintaining a very wide radiation pattern in frequency bands below 30 MHz. Informed by results from previous lunar missions, we create a simplified lunar soil model and simulate the membrane antenna performance when successfully deployed. On the lunar surface, the antenna efficiency is predicted to be greater than 10% at 5–35 MHz and greater than 90% at 12–19 MHz, with the radiation pattern maintaining a dipole form at 5–30 MHz. As noted in Section 3.3, for observations at such low frequencies, the sky temperature is very high, meaning that a 10% antenna efficiency is sufficient for astronomical observations with a good signal-to-noise ratio.

This study still has a number of limitations. It assumes the antenna membrane to be laid on a perfectly flat and uniform ground plane and adopts a highly simplified model for the lunar ground. In reality, it is unlikely to be deployed on a flat surface, and a more complex distribution of subsurface material may be present. While we vary our ground model parameters, such more complicated cases are not considered here. Additionally, the membrane antenna itself may also have bends and folds. Such issues will be addressed in future work. Nevertheless, the work presented here provides a good foundation for the design of a lunar-based radio telescope and can be used to aid in the design of antenna arrays on the lunar far side.

## ACKNOWLEDGEMENTS

We acknowledge the support of the National SKA program of China (2022SKA0110100, 2022SKA0110101), and the Natural Science Foundation of China (12273070, 12203061, 1236114814, 12303004).

## AUTHOR CONTRIBUTIONS

Xuelei Chen conceived the basic idea of the project, Fengquan Wu guided Suonanben to conduct the simulation and experimental work, and Tianlu Chen participated in the discussion. Kai He, Shijie Sun, Wei Zhou, Minquan Zhou, Cong Zhang, Jiaqin Xu, Qisen Yan, Shenzhe Xu, Jiacong Zhu, Zhao Wang, Ke Zhang and Yougang Wang made contributions in field testing. Jixia Li provided support in data acquisition and storage. Haitao Miao offered assistance in programming and paper revision. All authors read and approved the final manuscript.

## DECLARATION OF INTERESTS

Xuelei Chen is an editorial board member for Astronomical Techniques and Instruments and he was not involved in the editorial review or the decision to publish this article. The authors declare no competing interests.

### REFERENCES

[1] Gorgolewski, S. 1966. Lunar Radio Astronomy Observatory. In Proceedings of the 1st Lunar International Laboratory (LIL) Symposium on Research in Geosciences and Astronomy.

[2] Jester, S., Falcke, H. 2009. Science with a lunar low-frequency array: from the dark ages of the Universe to nearby exoplanets. *New Astronomy Reviews*, **53**(1): 1−26.

[3] Pritchard, J. R., Loeb, A. 2012. 21 cm cosmology in the 21st century. *Reports on Progress in Physics Physical Society*, **75**(8): 086901.

[4] Loeb, A., Zaldarriaga, M. 2004. Measuring the small-scale power spectrum of cosmic density fluctuations through 21 cm tomography prior to the epoch of structure formation. *Physical Review Letters*, **92**: 211301.

[5] Silk, J. 2021. The limits of cosmology: role of the Moon. *Philosophical Transactions of the Royal Society Series A*, **379**(2188): 20190561.

[6] Koopmans, L. V. E., Barkana, R., Bentum, M., et al. 2021. Peering into the dark (ages) with low-frequency space interferometers. *Experimental Astronomy*, **51**(3): 1641−1676.

[7] Chen, X. L., Burns, J., Koopmans, L., et al. 2019. Discovering the sky at the longest wavelengths with small satellite constellations. *arXiv:1907.10853*.

[8] Alexander, J. K., Kaiser, M. L., Novaco, J. C., et al. 1975. Scientific instrumentation of the Radio-Astronomy-Explorer-2 satellite. Astronomy and Astrophysics, 40(4):365−371.

[9] Zhu, X. Y., Su, Y., Ji, Y. C., et al. 2021. Ground

experiments and performance evaluation of the Low-Frequency Radio Spectrometer onboard the lander of Chang'e-4 mission. *Research in Astronomy and Astrophysics*, **21**(5): 116.

[10] Chen, L., Ping, J., Falcke, H., et al. 2020. The Netherlands-China Low Frequency Explorer (NCLE). Bulletin of the AAS, 52(3).

[11] Yan, J., Wu, J., Gurvits, L. I., et al. 2023. Ultra-low-frequency radio astronomy observations from a Selenocentric orbit. *Experimental Astronomy*, **56**(1): 333−353.

[12] Burns, J. O. 2021. Transformative science from the lunar farside: observations of the dark ages and exoplanetary systems at low radio frequencies. *Philosophical Transactions of the Royal Society A*, **379**(2188): 20190564.

[13] Chen, X. L., Yan, J. Y., Deng, L., et al. 2020. Discovering the Sky at the Longest wavelengths with a lunar orbit array. *Philosophical Transactions of the Royal Society A*, **379**: 20190566.

[14] Huang, Q. Z., Sun, S. J., Zuo, S. F., et al. 2018. An Imaging Algorithm for a Lunar Orbit Interferometer Array. *The Astronomical Journal*, **156**(2): 43.

[15] Shi, Y., Xu, Y. D., Deng, L., et al. 2021. Imaging sensitivity of a linear interferometer array on lunar orbit. *Monthly Notices of the Royal Astronomical Society*, **510**(2): 3046−3062.

[16] Chen, X. L., Yan, J. Y., Xu, Y. D., et al. 2023. Discovering the Sky at the longest wavelength mission−A pathfinder for exploring the cosmic dark ages. *Chinese Journal of Space Science*, **43**(1): 43−59.(in Chinese)

[17] Bale, S. D., Bassett, N., Burns, J. O., et al. 2023. LuSEE 'Night': The lunar surface electromagnetics experiment. *arXiv:2301.10345*.

[18] Bandyopadhyay, S., Mcgarey, P., Goel, A., et al. 2021. Conceptual design of the Lunar Crater Radio Telescope (LCRT) on the far side of the Moon. In 2021 IEEE Aerospace Conference (50100).

[19] Chen, X. L., Gao, F., Wu, F. Q., et al. 2024. Large-scale Array for Radio Astronomy on the Farside (LARAF). *Philosophical Transactions of the Royal Society A*, **382**: 20230094.

[20] Jones, D. L., Lazio, J., Giersch, L., et al. 2013. Low frequency antenna options for the lunar surface. In 2013 IEEE Aerospace Conference.

[21] Lichodziejewski, D., Cravey, R., Hopkins, G. 2003. Inflatably deployed membrane waveguide array antenna for space. In Proceedings of 44th AIAA/ASME/ASCE/AHS/ASC Structures, Structural Dynamics, and Materials Conference.

[22] Liu, Z. Q., Qiu, H., Li, X., et al. 2017. Review of Large Spacecraft Deployable Membrane Antenna Structures. *Chinese Journal of Mechanical Engineering*, **30**(6): 1447−1459.

[23] Adami, K. Z., Farhat, I. O. 2021. Low-frequency technology for a lunar interferometer. *Philosophical Transactions of the Royal Society Series A*, **379**(2188): 20190575.

[24] Scarpello, M. L., Kurup, D., Rogier, H., et al. 2011. Design of an implantable slot dipole conformal flexible antenna for biomedical applications. *IEEE Transactions on Antennas Propagation*, **59**(10): 3556−3564.

[25] Diaham, S. 2021. Polyimide in Electronics: Applications and processability overview. In Polyimide for Electronic and Electrical Engineering Applications. London: Intechopen.

[26] Chen, Z. N., Chia, M. Y. W. 2006. Broadband planar antennas: design and applications. Hoboken: John Wiley & Sons.

[27] Li, J. X., Zuo, S. F., Wu, F. Q., et al. 2020. The Tianlai Cylinder Pathfinder array: System functions and basic performance analysis. *Science China Physics, Mechanics & Astronomy*, **63**(12): 129862.

[28] Wraith, J. M., Or, D. 1999. Temperature effects on soil bulk dielectric permittivity measured by time domain reflectometry: Experimental evidence and hypothesis development. Water Resources Research, 35(2):361−369.

[29] Valdes, L. B. 1954. Resistivity measurements on germanium for transistors. *Proceedings of the IRE*, **42**(2): 420−427.

[30] Heiken, G., Vaniman, D., French, B. M. 1991. Lunar sourcebook-A user's guide to the moon. Cambridge: Cambridge University Press.

[31] Feng, J. Q, Siegler, M. A., White, M. N. 2022. Dielectric properties and stratigraphy of regolith in the lunar South Pole-Aitken basin: Observations from the Lunar Penetrating Radar. *Astronomy & Astrophysics*, **661**: A47.

[32] Ding, C. Y., Xiao, Z. Y., Su, Y., et al. 2020. Compositional variations along the route of Chang'e-3 Yutu rover revealed by the lunar penetrating radar. *Progress in Earth and Planetary Science*, **7**: 32.

[33] Su, Y., Wang, R. G., Deng, X. J., et al. 2022. Hyperfine structure of regolith unveiled by Chang'E-5 Lunar Regolith Penetrating Radar. *IEEE Transactions on Geoscience and Remote Sensing*, **60**: 1−14.

[34] Mckay, D. S., Heiken, G., Basu, A., et al. 1991. The lunar regolith. In Lunar Sourcebook: A User's Guide to the Moon. Cambridge: Cambridge University Press.